Research paper

Unresolved MPS-DEM coupling method for three-dimensional liquid-solid dam-break flows impacting on rigid structures

Fengze Xie [a] , Guohua Pan [b], Weiwen Zhao [a] , Decheng Wan [a,*]

[a] *Computational Marine Hydrodynamics Lab (CMHL), School of Naval Architecture, Ocean and Civil Engineering, Shanghai Jiao Tong University, Shanghai, China*
[b] *Ningbo Pilot Station, Ningbo Dagang Pilotage Co., Ltd., Ningbo, China*

ARTICLE INFO

ABSTRACT

Liquid-solid dam-break flows widely occur in the ocean engineering field, which are more complicated and threaten the safety of nearshore structures. In this paper, a fully-Lagrangian multi-phase model, based on the Moving Particle Semi-implicit Method (MPS) and Discrete Element Method (DEM), is developed for the simulation of liquid-solid dam-break flows impacting the rigid structures. The local averaging technique is employed to describe the fluid motion both inside and outside the sediment and there are the so-called Model A and Model B for governing equations. Two cases of multiple particles sedimentation and two-phase dam-break are simulated first. The numerical results show that Model B performs better than Model A in the 3-D MPS-DEM method. Subsequently, the proposed method with Model B is used to investigate the liquid-solid dam-break flows colliding with the rigid structures.

1. Introduction

Dam-break flows carrying sediment pose a threat to the safety of offshore structures, such as bridge piers, breakwaters, legs of platform and etc. The impact force exerted on those structures is highly complex. The upper parts are impacted only by clear water, while the lower parts interact with the water-sediment mixture. Therefore, the ability to accurately predict the impact force is crucial for engineers to better design and optimise offshore structures. With the development of computer hardware, numerical techniques have become an effective complement to traditional experiments in the research of liquid-solid two-phase flows and have been widely accepted over the past several decades.

In the simulation of liquid-solid flows, solid phase can be modelled as either a whole continuum or discrete particles. The former is known as the Two Fluid Model (TFM), while the latter is based on the Discrete Element Method (DEM). TFM is widely used to simulate the large-scale two-phase flows (Jandaghian et al., 2021), but the motion behaviour of single particle is not taken into account. DEM, as a mature method, focuses on solid-solid interaction and can be coupled with either mesh-based methods or particle-based methods. The coupling strategy can be classified as resolved coupling and unresolved coupling. For resolved coupling methods, fine fluid grids or particles are needed and

hydrodynamic force exerted on the DEM particles is calculated through the integration (Sun et al., 2023, 2024). As a result, resolved coupling methods can describe the interaction between fluid and particles more accurately, while their computational cost is very high. By contrast, fewer fluid grids or particles are used in unresolved coupling methods. This coupling is achieved by the local average technique (Sun and Sakai, 2015; Tang et al., 2024) or Volume Averaged and Favre Averaged Navier-Stokes (VAFANS) equations (Hu et al., 2012; Ren et al., 2016; Wen et al., 2018), in which the information exchange between the fluid and DEM particles is calculated through empirical force laws.

Particle-based methods show their superiority in simulating free-surface flows with large deformation, such as dam-break flows. Gingold and Monaghan (1977) developed a Weakly Compressible Smoothing Particle Hydrodynamic (WCSPH) method, which was firstly used to solve astrophysical problems. Koshizuka and Oka (1996) proposed the incompressible Moving Particle Semi-implicit (MPS) method, a projection-based particle approach. These original particle-based methods had some drawbacks, such as in-stability and inefficiency. Therefore, a series of novel algorithms have been proposed to overcome these shortcomings. The gradient model of momentum conservation (Tanaka and Masunaga, 2010), the mixed source term of Pressure Poisson Equation (PPE) (Khayyer and Gotoh, 2011; Tanaka and Masunaga, 2010) and high order schemes (Khayyer and Gotoh, 2010, 2011,

---

2012) have been developed to find a compromise between accuracy and stability. The Particle Shifting Techniques (PST) (Duan et al., 2018; Gotoh et al., 2024; Khayyer et al., 2017, 2023; Liu et al., 2024; Lyu and Sun, 2022; Shimizu and Gotoh, 2024) have been proposed to prevent the particles from uneven distribution, which significantly improves the stability of incompressible particle-based method.

There are two sets of governing equations, models A and B, which are used for the unresolved coupling of DEM and other methods (Feng and Yu, 2004; Zhu et al., 2007). Model A assumes that the pressure drop is exchanged between the fluid phase and the solid phase, while Model B assumes that the pressure drop is exerted to fluid phase only. DEM has also been coupled with particle-based methods and these fully-Lagrangian coupling methods have been applied to complicated liquid-solid two-phase flows. Sun et al. (2013, 2014) coupled DEM with different particle-based methods, including SPH and MPS. The formulation of the governing equations for the fluid phase is based on Model A. These coupling methods have been successfully applied to the simulation of two-phase dam-break and two-phase flows in the rotating cylinder. Li et al. (2019) extended the MPS-DEM method to simulate the non-Newtonian solid-liquid flows with a free-surface. Model B is also used in the formulation of the governing equations for the fluid phase. He et al. (2018) adopted GPU acceleration technique to improve the efficiency of SPH-DEM model, which was used to simulate the agitated flows. Markauskas et al. (2018) employed the SPH-DEM coupling model to conduct the numerical analysis of wet plastic particle separation. Harada et al. (2019) developed a MPS-DEM coupling model to simulate the sediment transport process in the swash zone of the beach. Furthermore, Harada et al. (2018) employed this MPS-DEM coupling model to investigate the morphological dynamics of step-and-pool riverbeds, revealing the effects of water surface fluctuations on step formation/collapse. Tazaki et al. (2023) employed a 2D DEM-MPS coupled model to simulate the gravel sediment transport process on a sloped beach under regular waves. Tazaki et al. (2024) used a 3D MPS-DEM coupling model to investigate the mechanisms of turbulence budgets and sediment motion under plunging waves. In our previous work (Xie et al., 2021, 2022), the MPS-DEM method with Model B has been developed and applied for simulating the liquid solid flows in the hydraulic flows.

The merits and shortcomings of CFD-DEM (Eulerian-Lagrangian) unresolved coupling models with different formulations have been discussed in a previous article (Feng and Yu, 2004). In the specific simulation of gas fluidization of binary mixtures of particle, CFD-DEM with Model B performed better than Model A. Zhou et al. (2010) also summarized the coupling schemes of mesh-based method and DEM. It can be concluded that Model A is more suitable for complex fluid-particle two-phase flows than Model B. Although fully-Lagrangian unresolved coupling methods with different formulations have been widely used in the field of industry, the Model A and B have rarely been compared in detail.

There are two publications (Jin et al., 2023; Meng et al., 2022) related to liquid-solid dam-break flows impacting fixed structures. These simulations are carried out by the Eulerian-Lagrangian coupling method and Eulerian-Eulerian coupling method. The Fully-Lagrangian coupling methods based on different models have also been employed to investigate liquid-solid two-phase dam-break flows. The surface profile (Tang et al., 2018) and moving velocity of flows (Zhang et al., 2023) are focused on. However, the dynamic pressure load and water-sediment-structure interaction are rarely studied.

In this work, 3D MPS-DEM methods with governing equations that are Model A and Model B are developed. In the first section, the improved MPS method, the DEM method and their coupling algorithm with different formulations are briefly presented. In the second section, two numerical simulations are carried out by the 3D MPS-DEM methods. In the first example involving multi-particles sediment, the fluid pressure, the kinetic energy of solid particles and the fluid forces exerted on the sediment are recorded to assess the stability of 3D MPS-DEM models.

The second case involving liquid-solid two-phase dam-break flows is simulated to demonstrate the accuracy of 3D MPS-DEM methods. In the third section, numerical results of liquid-solid two-phase dam-break flows impacting fixed structures are presented and discussed. Finally, conclusions and future work are presented.

2. Numerical methods

2.1. Liquid phase

The liquid phase is simulated using the MPS by solving the local average governing equations (Anderson and Jackson, 1969). In previous studies, two formulations, referred to as Models A and B, were used. Model A assumes that the pressure drop is exchanged between the fluid phase and the solid phase, while Model B assumes that the pressure drop is exerted solely on the fluid phase. The corresponding governing equations for the fluid phase in liquid-solid flows can be written as,

Model A:

$$\frac{D\varepsilon_f \rho_f}{Dt} + \rho_f \nabla \bullet \boldsymbol{u}_d = 0 \tag{1}$$

$$\rho_f \frac{D\boldsymbol{u}_d}{Dt} = -\varepsilon_f \nabla P + \mu_f \nabla^2 \boldsymbol{u}_d - \boldsymbol{f}_A + \varepsilon_f \rho_f \boldsymbol{g} \tag{2}$$

Model B:

$$\frac{D\varepsilon_f \rho_f}{Dt} + \rho_f \nabla \bullet \boldsymbol{u}_d = 0 \tag{3}$$

$$\rho_f \frac{D\boldsymbol{u}_d}{Dt} = -\nabla P + \mu_f \nabla^2 \boldsymbol{u}_d - \boldsymbol{f}_B + \varepsilon_f \rho_f \boldsymbol{g} \tag{4}$$

where subscript f represents the fluid particle. ε_f, ρ_f, P, μ_f, $\boldsymbol{g}$ and t denote the porosity, the fluid density, the pressure, the dynamic viscosity, the gravity acceleration vector and the physical time, respectively. $\boldsymbol{u}_d$ ($\boldsymbol{u}_d = \varepsilon_f \boldsymbol{u}_f$) is the Darcy velocity and $\boldsymbol{u}_f$ is the intrinsic velocity. $\boldsymbol{f}_A$ and $\boldsymbol{f}_B$ denote the body force due to the momentum exchange between solid phase and liquid phase. There is a relationship between $\boldsymbol{f}_A$ and $\boldsymbol{f}_B$, given by, $\boldsymbol{f}_B = \frac{\boldsymbol{f}_A}{\varepsilon_f} - \varepsilon_s \rho_f \boldsymbol{g}$ (Feng and Yu, 2004). ε_s represents the porosity of solid. Therefore, Eq. (4) can be re-written as,

$$\rho_f \frac{D\boldsymbol{u}_d}{Dt} = -\nabla P + \mu_f \nabla^2 \boldsymbol{u}_d - \frac{\boldsymbol{f}_A}{\varepsilon_f} + \rho_f \boldsymbol{g} \tag{5}$$

The interaction between MPS particles is governed by a kernel function $w(r)$, which plays a role of weight function in the discretization process. In order to avoid non-physical pressure oscillations, the kernel function presented by Zhang et al. (2014) is employed here, given by,

$$w(r) = \begin{cases} \dfrac{r_e}{0.85r + 0.15r_e} - 1 & 0 \leq r < r_e \\ 0 & r \geq r_e \end{cases} \tag{6}$$

where r represents the distance between two MPS particles, and r_e is the radius of particles interaction. r_e is set to 4.1 r_0, where r_0 is the initial particle spacing.

The number density reflects the distribution of fluid particles. In the liquid-solid two-phase model (Pahar and Dhar, 2017), the number density can be modified as,

$$\langle n \rangle_i = \sum_{j \neq i} \frac{w(|\boldsymbol{r}_j - \boldsymbol{r}_i|)}{\varepsilon_j} \tag{7}$$

where subscripts i and j are the MPS fluid particles, $\boldsymbol{r}_i$ is the position vector relative to origin, ε_j is the porosity of MPS particle j.

The particle interaction models contain gradient model, divergence model and Laplacian model, given by,

$$\langle \nabla \phi \rangle_i = \frac{d}{n^0} \sum_{j \neq i} \frac{\phi_j + \phi_i}{|\mathbf{r}_j - \mathbf{r}_i|^2} (\mathbf{r}_j - \mathbf{r}_i) \frac{w(|\mathbf{r}_j - \mathbf{r}_i|)}{\varepsilon_j} \tag{8}$$

$$\langle \nabla \bullet \mathbf{\Phi} \rangle_i = \frac{d}{n^0} \sum_{j \neq i} \frac{(\mathbf{\Phi}_j - \mathbf{\Phi}_i) \bullet (\mathbf{r}_j - \mathbf{r}_i)}{|\mathbf{r}_j - \mathbf{r}_i|^2} \frac{w(|\mathbf{r}_j - \mathbf{r}_i|)}{\varepsilon_j} \tag{9}$$

$$\langle \nabla^2 \phi \rangle_i = \frac{2d}{n^0 \lambda} \sum_{j \neq i} (\phi_j - \phi_i) \frac{w(|\mathbf{r}_j - \mathbf{r}_i|)}{\varepsilon_j} \tag{10}$$

$$\lambda = \frac{\sum_{j \neq i} w(|\mathbf{r}_j - \mathbf{r}_i|) |\mathbf{r}_j - \mathbf{r}_i|^2}{\sum_{j \neq i} w(|\mathbf{r}_j - \mathbf{r}_i|)} \tag{11}$$

where ϕ is the physical quantities of MPS particles, d is the number of space dimensions, λ is a parameter which is used to make the variance increase equal to the analytical solution.

In MPS method, the pressure field is obtained by solving Poisson Pressure Equation (PPE). Mixed source term method (Khayyer and Gotoh, 2011; Tanaka and Masunaga, 2010) is adopted in this work, given by,

Model A:

$$\langle \nabla^2 p^{m+1} \rangle_i = (1 - \gamma) \frac{\rho_f}{\Delta t} \nabla \bullet \mathbf{u}_i^* - \gamma \frac{\rho_f}{\Delta t^2} \frac{\langle n^m \rangle_i - n^0}{n^0} \tag{12}$$

Model B:

$$\langle \nabla^2 p^{m+1} \rangle_i = (1 - \gamma) \frac{\varepsilon_f \rho_f}{\Delta t} \nabla \bullet \mathbf{u}_i^* - \gamma \frac{\varepsilon_f \rho_f}{\Delta t^2} \frac{\langle n^m \rangle_i - n^0}{n^0} \tag{13}$$

where γ is the weight parameter and its value is set to 0.01 in this paper.

The free surface detection method based on the asymmetry distribution of neighbouring particles is employed here, given by,

$$\langle n \rangle_i^* \langle \beta n_0 \tag{14}$$

$$\langle \mathbf{F} \rangle_i = \frac{d}{n^0} \sum_{j \neq i} \frac{(\mathbf{r}_j - \mathbf{r}_i)}{|\mathbf{r}_j - \mathbf{r}_i|} \frac{w(|\mathbf{r}_j - \mathbf{r}_i|)}{\varepsilon_j} \tag{15}$$

$$\langle \mathbf{F} \rangle_i > \alpha |\mathbf{F}^0| \tag{16}$$

where $\mathbf{F}$ is the vector which represents the asymmetry distribution of MPS neighbour particles. $\mathbf{F}^0$ is the $\mathbf{F}$ of the internal fluid particles at initial time. Parameters β and α are set to 0.8 and 0.9, respectively.

2.2. Solid phase

The discrete solid particles are modelled by DEM, which is governed by Newton's second law, given by,

$$m_k \frac{D\mathbf{v}_k}{Dt} = \sum_l \mathbf{F}_{kl}^C + m_k \mathbf{g} + \mathbf{F}_k^{\text{int}} \tag{17}$$

$$I_k \frac{D\boldsymbol{\omega}_k}{Dt} = \sum_l \mathbf{M}_{kl}^C \tag{18}$$

where the subscripts k and l represent the DEM particles that are in contact with each other. m_k, I_k, $\mathbf{v}_k$ and $\boldsymbol{\omega}_k$ are the mass, the moment of inertia, the translational velocity, and rotational velocities of DEM particle k, respectively. $\mathbf{F}_{kl}^C$ and $\mathbf{M}_{kl}^C$ are the contact force and moment, respectively. $\mathbf{F}_k^{\text{int}}$ is the hydrodynamic force exerted on the DEM particles.

The DEM particles can be regarded as soft spheres (Cundall and Strack, 1979), and the contact force is determined by the overlapping parts. The contact model includes dashpots, springs and sliders. The contact force $\mathbf{F}_{kl}^C$ can be decomposed into the normal and tangential

components. the normal force $\mathbf{F}_{kl}^{C,n}$ is given by,

$$\mathbf{F}_{kl}^{C,n} = -\chi^n \boldsymbol{\delta}_{kl}^n - \eta^n \mathbf{v}_{kl}^n \tag{19}$$

where $\boldsymbol{\delta}_{kl}^n$ and $\mathbf{v}_{kl}^n$ are the relative displacement and velocity in the normal direction. χ and η represent the spring stiffness and damping coefficient, respectively. The tangential force is given by,

$$\mathbf{F}_{kl}^{C,t} = \begin{cases} -\chi^t \boldsymbol{\delta}_{kl}^t - \eta^t \mathbf{v}_{kl}^t & |\mathbf{F}_{kl}^{C,t}| \leq \mu_s |\mathbf{F}_{kl}^{C,n}| \\ -\mu_s |\mathbf{F}_{kl}^{C,n}| \frac{\boldsymbol{\delta}_{kl}^t}{|\boldsymbol{\delta}_{kl}^t|} & |\mathbf{F}_{kl}^{C,t}| > \mu_s |\mathbf{F}_{kl}^{C,n}| \end{cases} \tag{20}$$

where $\boldsymbol{\delta}_{kl}^t$ and $\mathbf{v}_{kl}^t$ represent the relative displacement and velocity in the tangential direction. μ_s is the friction coefficient.

The normal spring stiffness χ^n (Bu et al., 2022) can be calculated as,

$$\chi^n = \frac{\sqrt{2}}{3} \frac{E}{(1 - \nu_s^2)} \sqrt{R} \tag{21}$$

where ν_s and R are the Poisson's ratio and the radius of solid particles. The tangential spring stiffness χ^t (Yu et al., 2023) can be calculated as,

$$\chi^t = \frac{\chi^n}{(2 + \nu_s)} \tag{22}$$

The damping coefficient (Zhang et al., 2009) is given by,

$$\eta^n = -2 \ln (e) \left(\sqrt{\frac{\chi^n m}{\ln^2 (e) + \pi^2}} \right) \tag{23}$$

$$\eta^t = -2 \ln (e) \left(\sqrt{\frac{\chi^t m}{\ln^2 (e) + \pi^2}} \right) \tag{24}$$

where e is the coefficient of restitution.

2.3. Liquid-solid interaction

The fluid forces exerted on DEM particles include the drag force, pressure gradient force, virtual mass force, and lubrication force. Because the drag force and pressure gradient force dominate (Sakai et al., 2012), other forces are not considered in present work.

The empirical drag force $\mathbf{F}_k^d$ is calculated as,

$$\mathbf{F}_k^d = \frac{\beta_k}{1 - \varepsilon_k} (\mathbf{u}_k - \mathbf{v}_k) V_k \tag{25}$$

where V_k and ε_k are the volume and the porosity of solid particle k. $\mathbf{u}_k$ is the fluid velocity in the centre of solid particle k. Two drag models of Ergun (1952) and Wen and Yu (1966) are combined. The coefficient of the interphase momentum exchange β_k is given by,

$$\beta_k = \begin{cases} 150 \frac{(1 - \varepsilon_k)^2}{\varepsilon_k} \frac{\mu_f}{d_k^2} + 1.75(1 - \varepsilon_k) \frac{\rho_f}{d_k} |\mathbf{u}_k - \mathbf{v}_k| & \varepsilon_k \leq 0.8 \\ 0.75 C_d \frac{\varepsilon_k (1 - \varepsilon_k)}{d_k} \rho_f \varepsilon_k^{-2.65} |\mathbf{u}_k - \mathbf{v}_k| & \varepsilon_k > 0.8 \end{cases} \tag{26}$$

where d_k represent the diameter of the DEM particle k. C_d is the drag coefficient, written as,

$$C_d = \begin{cases} \frac{24}{\text{Re}_k} \left(1 + 0.15 \text{Re}_k^{0.687} \right) & \text{Re}_k \leq 1000 \\ 0.44 & \text{Re}_k > 1000 \end{cases} \tag{27}$$

The Reynolds number in the centre of DEM particle k is defined as,

$$\text{Re}_k = \frac{\varepsilon_k \rho_f d_k |\mathbf{u}_k - \mathbf{v}_k|}{\mu_f} \tag{28}$$

Another weight function $w_s(r)$ (Sun et al., 2014) is employed to build the fluid-particle interaction, given by,

$$w_s(r) = \begin{cases} 4\left(\dfrac{r}{r_e}\right)^5 - 5\left(\dfrac{r}{r_e}\right)^4 + 1 & r < r_e \\ 0 & r \geq r_e \end{cases} \tag{29}$$

As it is integrable across the whole domain, a normalizer can then be calculated analytically, given by,

$$n_s = \int_0^\infty W_s(|\boldsymbol{r}_{ik}|) \bullet 4\pi r^2 dr = \frac{10\pi}{21} r_e^3 \tag{30}$$

Furthermore, the porosity of fluid particle i can be calculated as,

$$\varepsilon_i = 1 - \frac{1}{n_s} \sum_k w_s(|\boldsymbol{r}_{ik}|) V_k \tag{31}$$

The porosity and fluid velocity in the centre of DEM particle k are calculated by neighbouring MPS particles with the weight function w_s, given by,

$$\varepsilon_k = \frac{\sum\limits_i \varepsilon_i w_s(|\boldsymbol{r}_{ki}|)}{\sum\limits_i w_s(|\boldsymbol{r}_{ki}|)} \tag{32}$$

$$\boldsymbol{u}_k = \frac{\sum\limits_i \boldsymbol{u}_i w_s(|\boldsymbol{r}_{ki}|)}{\sum\limits_i w_s(|\boldsymbol{r}_{ki}|)} \tag{33}$$

the total hydrodynamic force exerted on the DEM particles can be written as,

Model A:

$$\boldsymbol{F}_k^{\text{int}} = \boldsymbol{F}_k^d - V_k \nabla P \tag{34}$$

Model B:

$$\boldsymbol{F}_k^{\text{int}} = \frac{\boldsymbol{F}_k^d}{\varepsilon_k} - V_k \rho_f \boldsymbol{g} \tag{35}$$

The reaction force exerted on the MPS particles is required to satisfy the momentum conservation law, given by,

$$\boldsymbol{f}_{A,i} = \frac{1}{V_i} \sum_k \boldsymbol{F}_k^d \left(\frac{w_s(|\boldsymbol{r}_{ki}|)}{\sum\limits_j w_s(|\boldsymbol{r}_{ki}|)} \right) \tag{36}$$

2.4. Time step

The incompressible MPS is a semi-implicit time-stepping approach, whereas DEM is an explicit one. Typically, the time step in DEM simulations is significantly smaller than that in MPS simulations. To ensure the stability of the simulation, a relatively small time step is chosen for the MPS-DEM coupling method, which, however, leads to high computational costs. In this study, the Modified Sequential Staggered (MSS) coupling algorithm for varying time steps (Sun et al., 2021) is utilised for both of these methods to address this issue.

The time step of MPS needs to fulfill the Courant - Friedrichs - Lewy (CFL) condition, which is expressed as,

$$\frac{u_{f,\max} \Delta t_{\text{mps}}}{dp} < C \tag{37}$$

where $u_{f,\max}$, Δt_{mps}, dp and C denote the maximum velocity of fluid particles, the time step, the initial particle spacing and the courant number, respectively.

The time step of DEM (Thornton and Randall, 1988) is determined by,

$$\Delta t_{\text{DEM}} < \frac{\pi R_{\min}}{0.01631\nu_s + 0.8766} \sqrt{\frac{2\rho_s(1 + \nu_s)}{E_s}} \tag{38}$$

where $R_{\min}$, ρ_s and E_s are the minimum radius, density and the elastic modulus of DEM solid particles, respectively.

3. Model verification

3.1. Multiple particle sedimentation

In this subsection, multiple particle sedimentation is simulated using 3D MPS-DEM methods with models A and B, firstly. Some model parameters used in different simulations in this study are the same, and they are summarized in Table 1. The size of the rectangular container is 0.05m × 0.1m × 0.15m. The water depth is 0.1 m, and 7425 solid particles are generated in the tank before the simulation. Fig. 1 shows the initial distribution of MPS particles and DEM particles. The solid particle group is distributed in the form of a simple cubic and about one MPS particle spacing away from the bottom of the water tank. After a period of time, due to the gravity of the particles themselves and the non-physical pressure oscillation disturbance, the particles will settle to the bottom and distribute more compactly.

In theory, the whole system will reach an equilibrium state in the end.

Fig. 2 shows the velocity field of solid particles at $t = 0.45$s. It can be noticed that some solid particles still exhibit velocity in the numerical results with Model A, whereas most solid particles have velocities near zero in those with Model B. Fig. 3 presents the time histories of kinetic energy. The total kinetic energy of solid particles can be calculated as, $E_k = \sum_k \frac{1}{2} m_k |\boldsymbol{v}_k|^2$. A similar phenomenon can be observed as that in Fig. 3. In the numerical results with Model A, the total kinetic energy of solid particles increases gradually after $t = 0.3$s. In the numerical results with Model B, the total kinetic energy of solid particles gradually decreases and tends towards zero. Fig. 4 shows the time histories of pressure measured by the probe located at the centre of the bottom. The pressure oscillates more violently in the numerical result with Model A than that in the numerical result with Model B. Besides, the pressure with Model B is closer to the analytic solution. The magnitudes of fluid forces exerted on the sediment are presented in Fig. 5. Theoretically, the whole system of liquid-solid two-phase will reach balance, and the relative velocity between fluid and solid will become zero in the end. Therefore, the magnitude of drag force exerted on the whole solid system should approach zero. Besides, the pressure gradient force should be equal to the buoyancy of solid particles in the still water. It can be noticed that the drag force with Model B tends to be zero after $t = 0.3$s, while the drag force with Model A continues to increase after $t = 0.3$s. The pressure gradient force with Model A does not tend to a constant value and oscillates with high frequency.

Table 1
Parameters in the simulations.

Fluid phase	Values
Density (kg/m³)	1000
Kinematic viscosity (m²/s)	1.0×10^{-6}
Initial particle distance (m)	0.0027
Time step(s)	1.0×10^{-4}

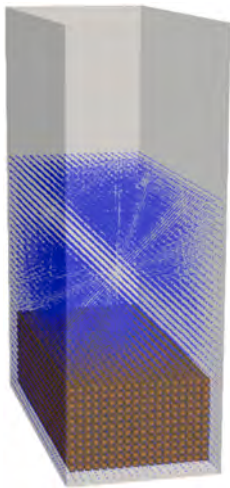| Solid phase	Values
Density (kg/m³)	2500
Radius (m)	0.00135
Young's modulus (N/m²)	1.0×10^8
Poisson's ratio	0.2
friction coefficient	0.2
Coefficient of restitution	0.9
Time step(s)	1.0×10^{-6}

Fig. 1. Initial distribution of MPS particles and DEM particles - multiple particle sedimentation.
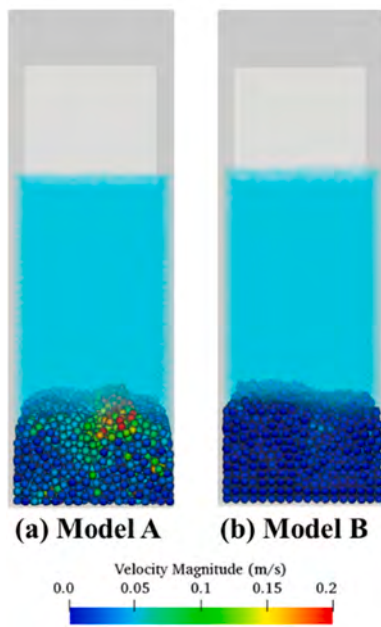
Fig. 2. Velocity field of solid particles at $t = 0.45s$ - multiple particle sedimentation.
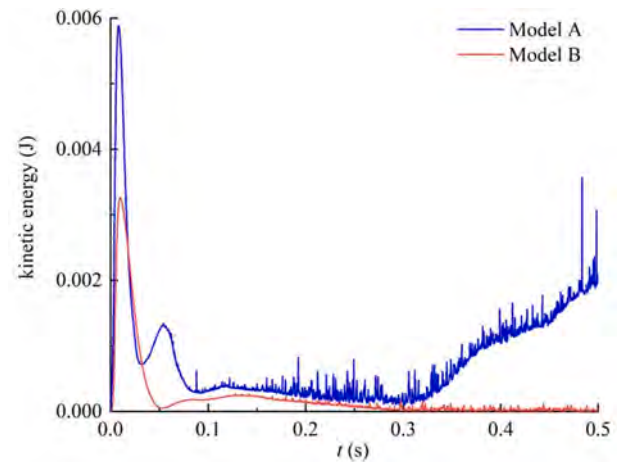

Fig. 3. Time histories of kinetic energy of solid particles - multiple particle sedimentation.
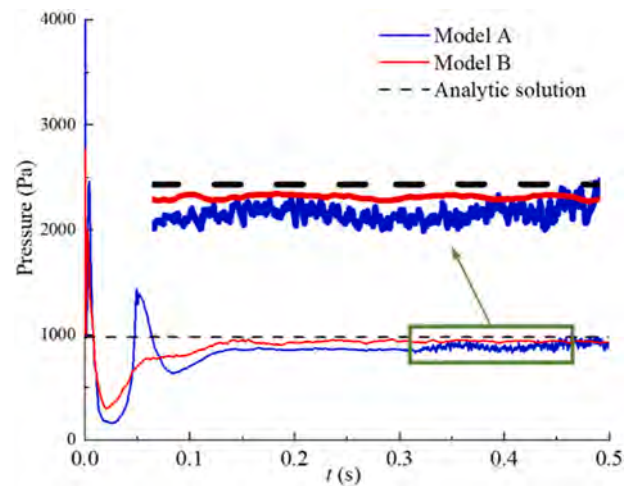

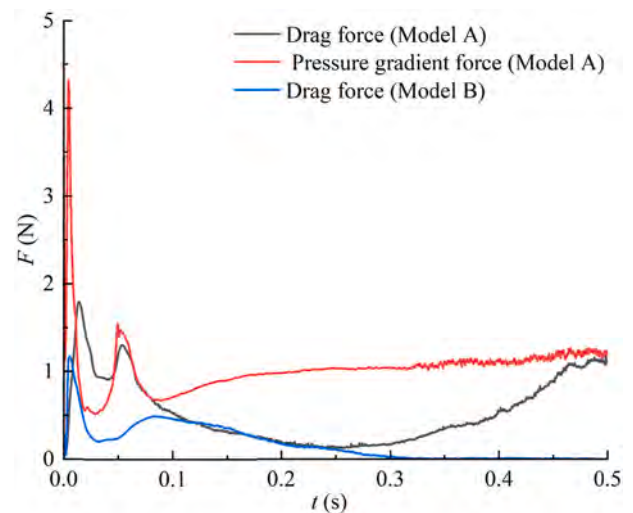**Fig. 4.** Time histories of pressure at the centre of bottom - multiple particle sedimentation.

Fig. 5. Time histories of the magnitudes of fluid forces exerted on the sediment - multiple particle sedimentation.
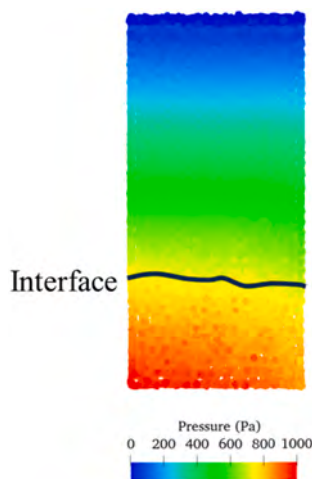
In general, the MPS-DEM method with Model B performs better than that with Model A. This is because the gradient term, which is not stable enough, is replaced by other equivalent term in the MPS-DEM method with Model B.

In addition to the pressure probe arranged at the bottom centre, pressure probes are also arranged at equal intervals on the side walls of the water tank. Figs. 6 and 7 present the pressure distriubtion of flow field by 3-D MPS-DEM (Model B). It can be noticed that the pressure field near the interface does not oscillate violently and the numerical results are in good agreement with the analytical solutions.

3.2. Liquid-solid two-phase dam-break flows

Liquid-solid two-phase dam-break was simulated in this subsection. The numerical results are compared with experimental data (Sun et al., 2013) to verify the accuracy of the 3D MPS-DEM method. The length of the rectangular container is 0.2m. its width and height are 0.1m and

Fig. 6. Pressure field at $t = 0.45$ s by 3-D MPS-DEM (Model B) - multiple particle sedimentation.
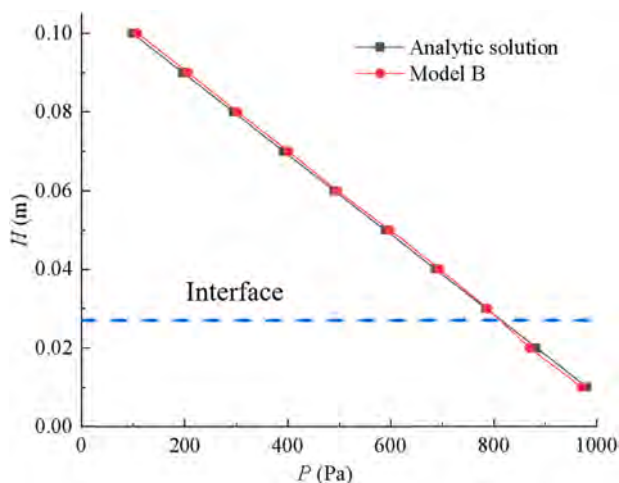

Fig. 7. Pressure distribution along the y-direction by 3-D MPS-DEM (Model B) - multiple particle sedimentation.

0.15m, respectively.

Fig. 8 shows the comparison between the simulation snapshots by MPS-DEM with Model A, MPS-DEM with Model B, and experimental photos (Sun et al., 2013). Figs. 9 and 10 present the shape of solid sediment and the free surface. It can be noted that both the shape of the sediment and the profile of the free-surface with Model B are in good agreement with those in experiment. In the numerical results with Model A, the sediment moves faster than the fluid, and its surface is not very smooth, which is different from what is observed in the experiment.

Figs. 11 and 12 present the time histories of the leading front of the liquid-solid flows. It can be noticed that the numerical results with Model B match well with experimental data. Some larger discrepancies of the leading front of the sediment between the numerical results with Model A and experimental data can be observed. The solid sediment in the simulation with Model A moves faster than its counterpart in the experiment, especially in the second half. The above analysis of the numerical results implies that the pressure oscillation significantly impacts the movement of solid particles in 3D MPS-DEM with Model A.

Additional simulations with initial MPS particle spacing (dp) being 0.002 m and 0.003 m are also conducted to verify the convergency of 3D MPS-DEM with model B. Figs. 13 and 14 present the time histories of the leading front of the fluid phase and the solid bed with different MPS resolutions. It can be noticed that the numerical results with different

MPS resolutions are almost consistent, showing the stability of 3D MPS-DEM with model B.

Fig. 15 shows the snapshots of the fluid phase and the solid sediment by 3-D MPS-DEM (Model B) at $t = 0.15$ s. It can be noticed that the pressure field and the free surface of the numerical results with dp being 0.0027 m and 0.002 m is smoother than the numerical result with dp being 0.003 m.

The time overhead of each part in MPS-DEM (Model B) in one MPS time step is presented in Table 2. It can be noted that as the MPS resolution increases, the time overhead of the DEM and coupling parts does not increase significantly, while the time overhead of the MPS part increases significantly.

In general, MPS-DEM with Model B is significantly superior to MPS-DEM with Model A in terms of both stability and accuracy. Therefore, MPS-DEM with Model B will be used in subsequent numerical simulations.

4. Numerical results and discussion

4.1. Liquid-solid dam-break flows with a short obstacle

The impact of single-phase dam-break flows on a short obstacle was experimentally investigated by Kleefsman et al. (2005). The sketch of the model is shown in Fig. 16. The tank size is 3.22 m long, 1.0 m wide and 1.0 m high. There is a water column that is 1.228 m long, 1.0 m wide and 0.55 m high, restricted to the left side of the tank. A short obstacle with a length of 0.161 m, a width of 0.41 m, and a height of 0.161 m is fixed downstream of the water column. A wave height gauge and a pressure sensor are installed to monitor the wave height and water pressure, as shown in Fig. 16. On the basis of this experiment, Liquid-solid dam-break flows interacting with a short obstacle were investigated numerically. H_s represents the height of sediment. A sediment column (1.228 m $\times$ 1.0 m $\times$ H_S) is placed inside the water column. The MPS particle spacing is set to 0.02 m and the radius of solid particle is 0.0125 m. Other physical parameters are kept consistent with those in the liquid-solid two-phase dam-break flow simulation. Four simulations with $H_S = 0$ m, 0.071 m, 0.113 m, and 0.152 m are conducted. The corresponding numbers of solid particles are 0, 5760, 9600, and 13440, respectively.

Fig. 17 presents the simulation snapshots of liquid-solid dam-break flows with various H_S. It can be noticed that before the dam-break flows impact the obstacle, the wave front of water propagates faster as H_S decreases. Besides, the more solid particles there are, the faster the sediment front moves, and the smaller the velocity difference between the water front and sediment front is. When the dam-break flows impact the obstacle, water splashing is generated. The splashing observed in the clear water case is stronger than that in the water-sediment cases. Some of the water carrying the solid particles passes through the sides of the obstacle and impacts the left wall. The reflected water forms a wave propagating towards the right wall.

Fig. 18 presents the hydrodynamic load exerted on the square obstacle. It can be observed that in the case with more solid particles, both the hydrodynamic force and pressure exerted on the square obstacle are detected later, and the peak values of the detected hydrodynamic force and pressure are also smaller. The main reason is that during the energy exchange between the fluid and the particles, the liquid transfers part of its kinetic energy to the solid particles. For the time interval when t is greater than 3.5s and less than 4.5s, the pressure detected at point P1 shows a downward trend in all cases. Besides, the fewer solid particles there are, the smaller the pressure detected at point P1 is. For the time interval when t is greater than 4.5s and less than 6.0s, the fewer solid particles there are, the earlier and the greater hydrodynamic and pressure peaks are detected.

Fig. 19 exhibits the time histories of loads of solid particles exerted on the square obstacle in the X direction. It can be noticed that the curve variation tendencies are similar. However, there are still some
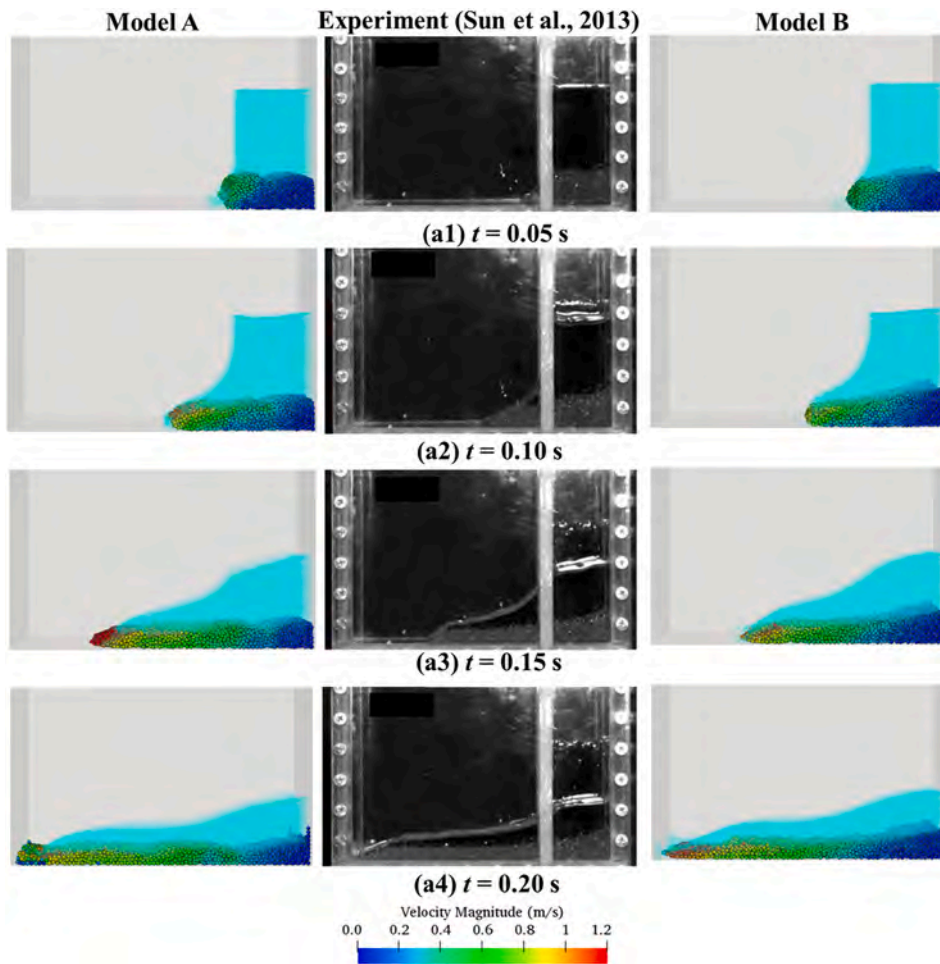
Fig. 8. Comparison between the simulation snapshots by MPS-DEM with Model A, MPS-DEM with Model B, and experimental photos (Sun et al., 2013) - liquid-solid two-phase dam-break flows.
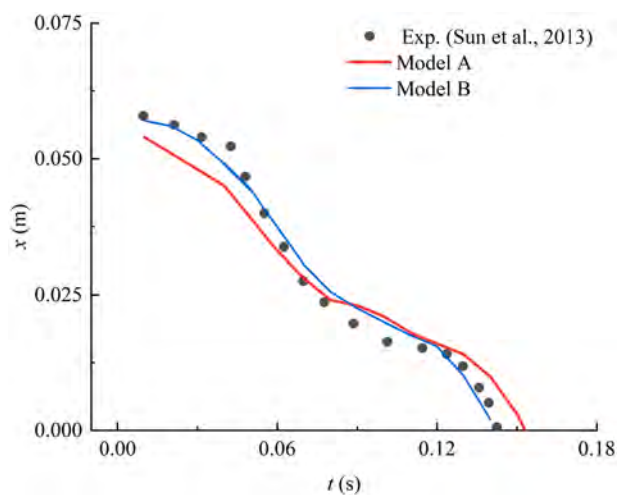

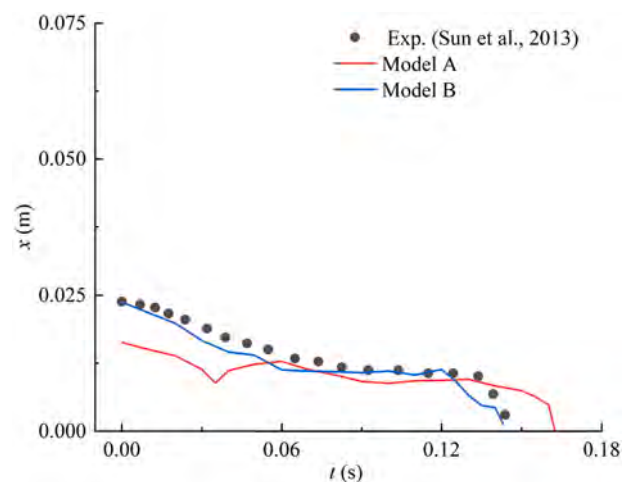**Fig. 9.** The shape of the free surface at $t = 0.1$s with different models - liquid-solid two-phase dam-break flows.

Fig. 10. The shape of the solid sediment at $t = 0.15$s with different models - liquid-solid two-phase dam-break flows.

differences in various cases, including the peak response time and peak value. In the case with the largest number of solid particles, the pressure peak is detected the earliest, and the peak value is the highest.

Fig. 20 presents the wave height time histories at H1. It can be noted that the tendencies of the curve's variations are not highly similar. At

times less than 3 s, two peaks are observed in the cases with pure water and initial sediment heights of 0.071m, while in the cases with initial heights of 0.113m and 0.152m, only a single peak is observed.

Fig. 21 presents propagations of the water front and the sediment front in simulated cases. It can be observed that solid sediments slow down the velocity of water. As the number of solid particles increases,
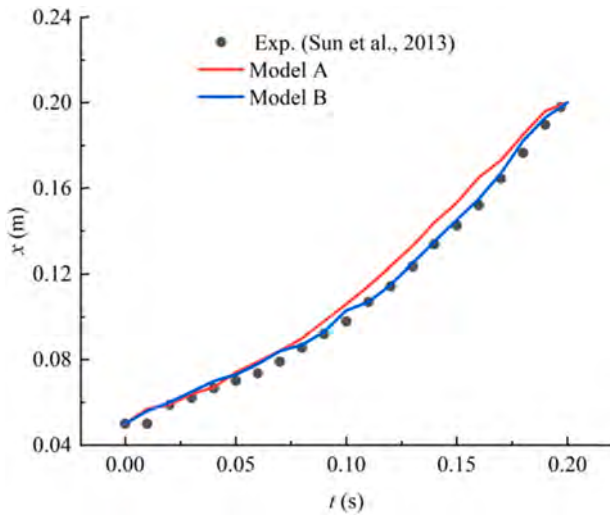
Fig. 11. Time histories of the leading front of the fluid flows with different models - liquid-solid two-phase dam-break flows.
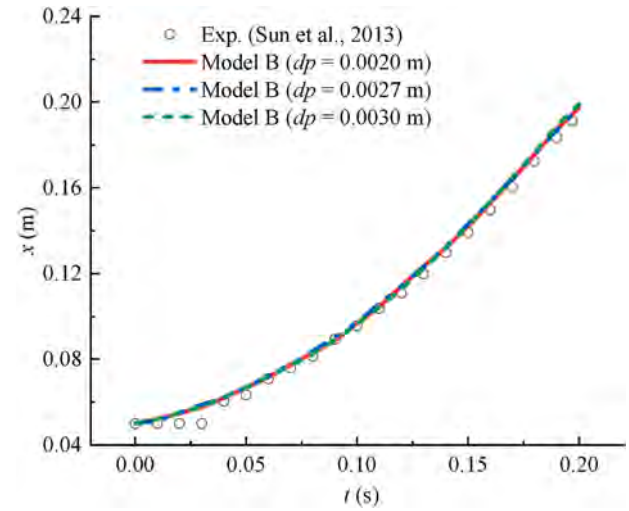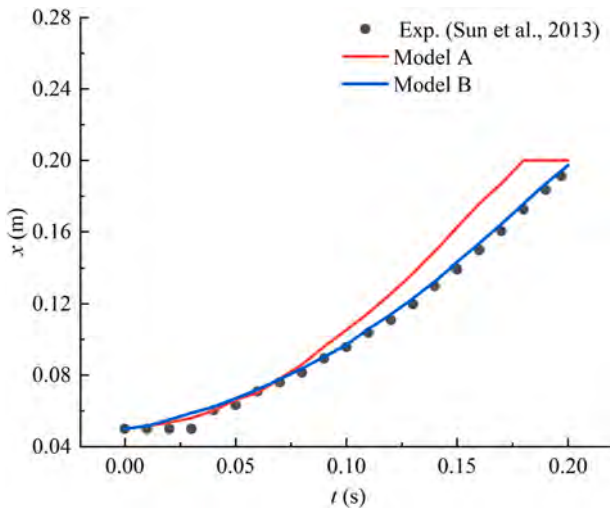

Fig. 12. Time histories of the leading front of the solid sediment with different models - liquid-solid two-phase dam-break flows.
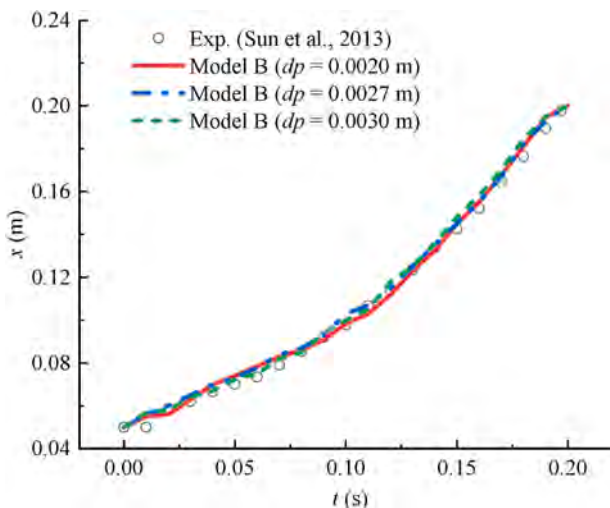

Fig. 13. Time histories of the leading front of the fluid flows by 3-D MPS-DEM (Model B) with different resolutions - liquid-solid two-phase dam-break flows.

Fig. 14. Time histories of the leading front of the solid sediment by 3-D MPS-DEM (Model B) with different resolutions - liquid-solid two-phase dam-break flows.

the velocity of water front decreases, while the velocity of the sediment front becomes higher. However, the velocity of the sediment front is always lower than that of the water. Furthermore, the more solid particles there are, the more synchronized the movement of the liquid front and the sediment front becomes.

4.2. Liquid-solid dam-break flows with a square column

Many marine structures, such as bridge piers and risers, can be simplified into square columns and vertical cylinders for research. In this subsection, the MPS-DEM coupling method is employed to simulate the liquid-solid dam-break flows impacting a square column. Fig. 22 presents the interactive model. The tank size is 1.6m long, 0.61m wide and 1.0m high. There is a water column, 0.4m long, 0.61m wide, and 0.3 m high, restricted to the left side of the tank by a baffle. A layer of water with a height of 0.01m is placed at the bottom of the tank on the right side of the baffle. A wave height gauge and a pressure sensor are arranged in the tank and on the square column, respectively, as shown in Fig. 22. The MPS particle spacing is set to 0.004 m and the radius of solid particle is 0.002 m. Other physical parameters are kept consistent with those in the liquid-solid two-phase dam-break flow simulation. Three simulations with sediment height H_S of 0m, 0.041m and 0.084m are carried out.

Fig. 23 presents snapshots of the interaction between the dam-break flow and a square obstacle at different liquid-solid ratios. At $t = 0.25$s, the two-phase fluid-particle dam-break flow has not yet reached the square column. Due to the presence of the bottom water layer, the liquid front of the dam-break flow is prone to rolling. It can be observed that, compared to the two-phase fluid-particle dam-break flow, the liquid front of the pure water dam-break flow is larger. This is because the solid particles slow down the velocity of the dam-break flow of liquid, making its interaction with the water layer less violent. At $t = 0.50$s, the central part of water climbs up along the square column. Due to the obstructive effect, the velocity of the particles located in the middle decreases rapidly and accumulates at the front of the square column. The liquid on both sides of the square column, carrying solid particles, continues to move forward, and a "cavity" forms behind the square column. At $t = 0.75$s, the fluid on both sides reaches the right wall of the water tank and climbs up. At the same time, the fluid on both sides, carrying a small amount of solid particles, moves into the "cavity." At $t = 1.00$s, the solid particles further fill the "cavity" behind the square column, and the shape of the "cavity" is triangular. Furthermore, it can be noted that the "cavity" is smaller and disappears more quickly in the cases with a larger
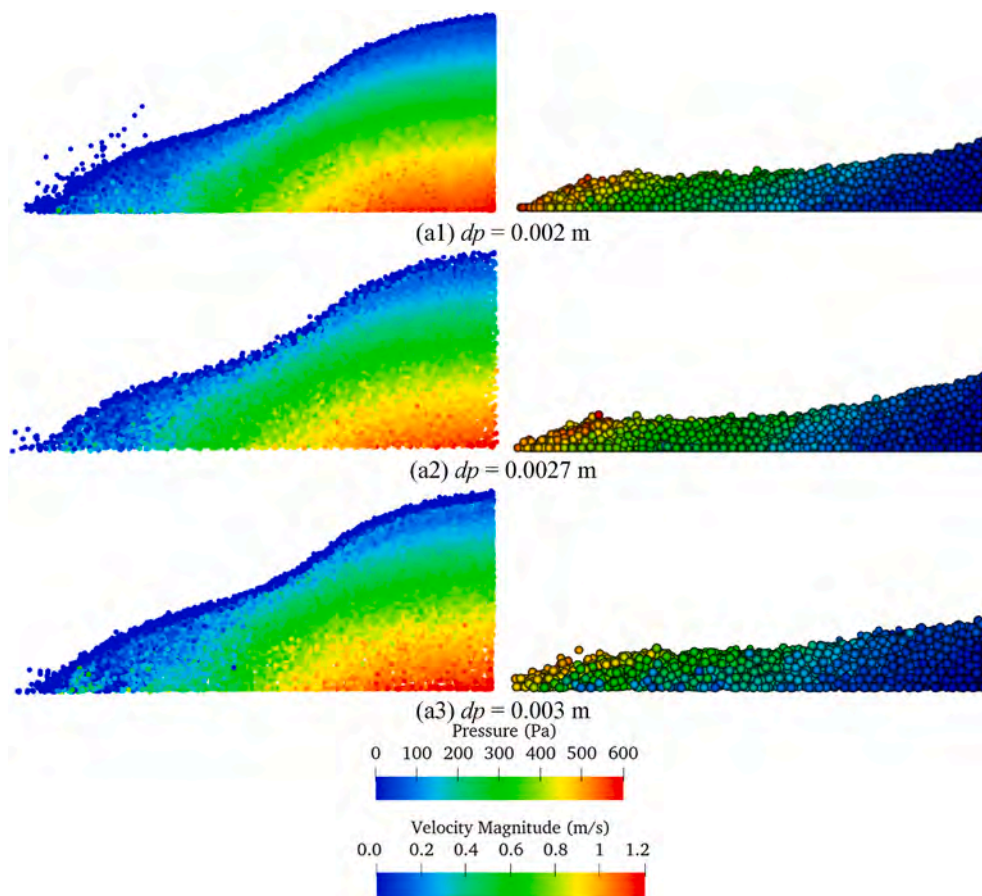
Fig. 15. Snapshots of the fluid phase and the solid sediment by 3-D MPS-DEM (Model B) with different MPS resolutions at $t = 0.15$ s - liquid-solid two-phase dam-break flows.

Table 2
Time consumed by each part of MPS-DEM (Model B) in one MPS time step - liquid-solid two-phase dam-break flows.

dp (m)	MPS part (s)	DEM and coupling parts (s)	Total (s)
0.002	4.40082	3.36281	7.76363
0.0027	1.83128	3.25171	5.08299
0.003	1.29677	3.24867	4.54544

initial sediment height. When $1.25s < t < 1.75s$, waves form and propagate towards the left side of the water tank. It can be observed that the more solid particles there are in the cases, the slower the wave propagation speed is. When $2.25s < t < 2.75s$, in the case with an initial sediment height $H_S = 0.084m$, the solid particles almost cover the bottom of the water tank; whereas in the case with an initial sediment height $H_S = 0.041m$, two small "cavities" form on.

Fig. 24 shows the time history of the hydrodynamic load exerted on the square column. In cases when the proportion of solid particles is higher, the hydrodynamic and pressure peaks are smaller and are detected at later times. When $0.35s < t < 1.25s$, the hydrodynamic and pressure loads detected in different cases decrease. When $1.25s < t < 2.00s$, the square column is subjected to reverse hydrodynamic force, and the hydrodynamic force increases rapidly, which corresponds to the impact effect between the waves reflected from the right wall and the back of the square column. Reflected waves propagate towards the left wall of the tank after passing by the square column, and the water level in front of the square column increases, hence the water pressure detected at point P1 increases. When $2.00s < t < 3.00s$, the hydrodynamic force exerted on the square column fluctuates around zero, with

smaller fluctuations observed in cases where there is a higher proportion of particles. The pressure detected at point P1 gradually decreases in different cases; meanwhile, the higher the proportion of particle quantity, the greater the detected pressure is, which corresponds to a higher water level near the probe.

Fig. 25 presents the loads of solid particles exerted on the square column in the X direction. In the case with more solid particles, the peak of the impact force on the square column is larger. Moreover, during the time interval $2.00s < t < 3.00s$, a significant reverse impact force of solid particles exerted on the square column can also be detected. In contrast, in the case with fewer particles ($H_S = 0.041m$), the reverse impact force of solid particles exerted on the square column is relatively smaller.

Fig. 26 illustrates the time histories of the wave height detected at point H1. As the liquid front passes the wave height gauge, the wave height gradually rises. During the time interval $0.3s < t < 0.7s$, the rate of water level rise at the wave height gauge slows down due to the gradual decrease of inflow. The dam break flow climbs up along the square column. Under the influence of gravity, the water overturns and forms waves, causing the water level at the gauge to rise rapidly. In the case with pure water, the water level rises most quickly; whereas in the case with the largest number of solid particles, the water level rises most slowly. The waves reflected by the square column then further move towards the left wall of the tank, leading to a decrease of water level at the wave height gauge. At around $t = 1.50s$, the waves reflected by the right wall of the tank reach the wave height gauge, causing the water level to rise again. When $1.50s < t < 3.00s$, it can be observed that there are multiple fluctuations, indicating that several waves have passed through the gauge. The most number of fluctuations and the largest fluctuation amplitude can be observed in the case with pure water. In contrast, there are relatively fewer fluctuations and smaller fluctuation
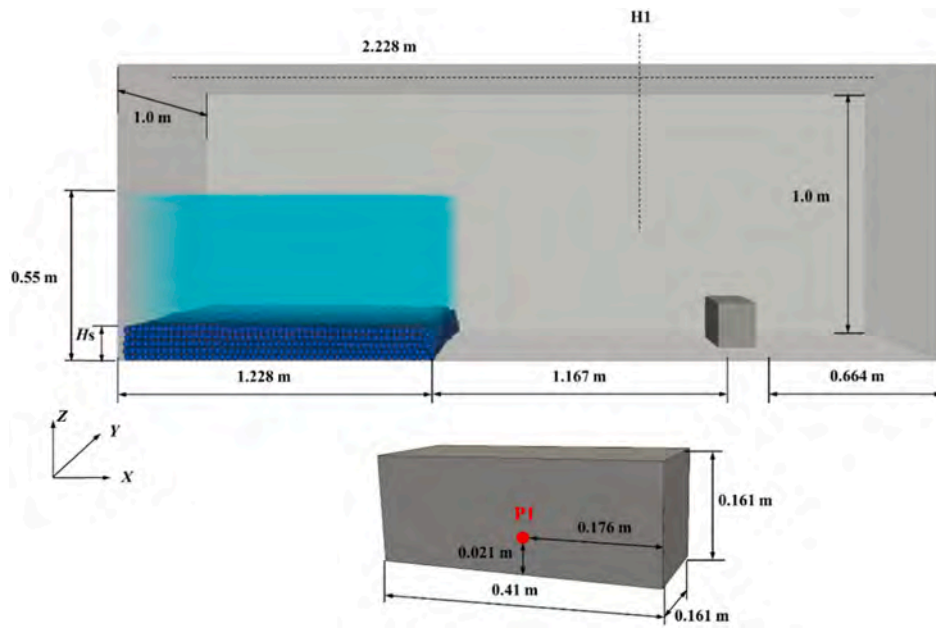
Fig. 16. The sketch of the model - liquid-solid dam-break flows with a short obstacle.
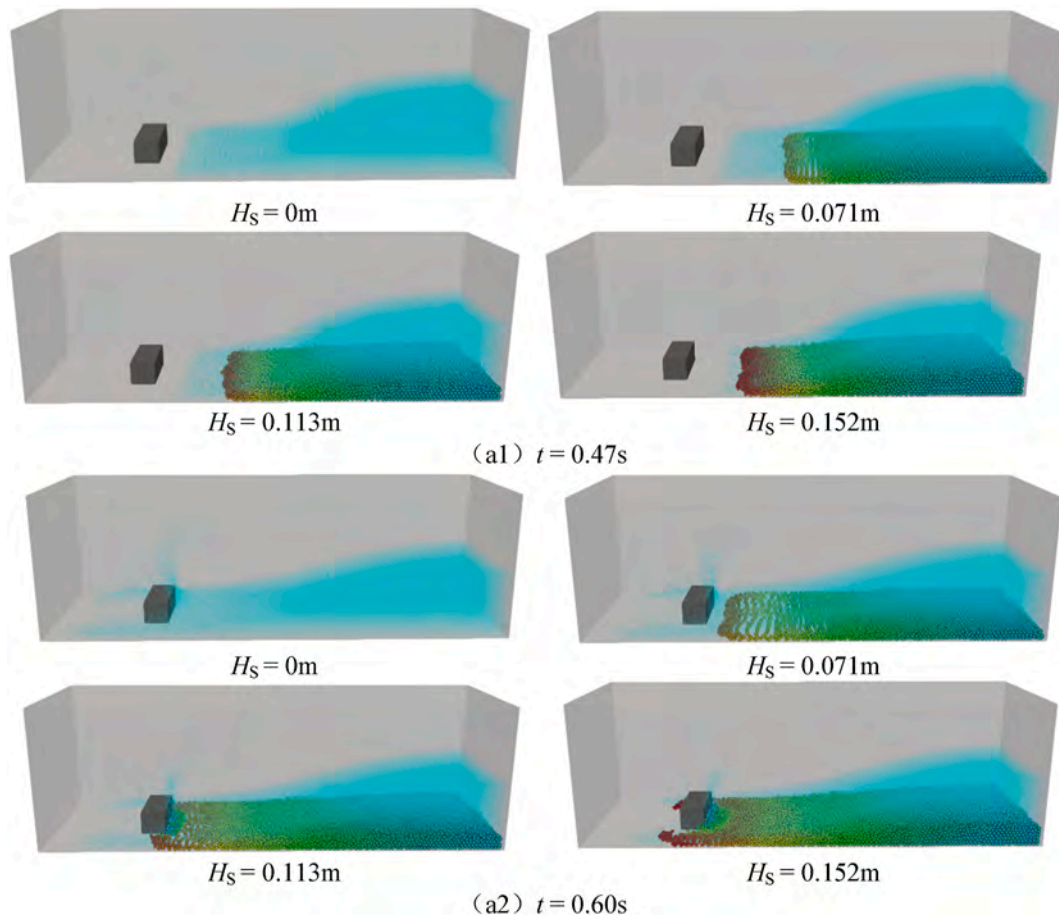

Fig. 17. Comparison of simulation snapshots of dam-break flows with different H_S - liquid-solid dam-break flows with a short obstacle.

amplitudes in the cases with solid particles. In summary, solid particles can significantly reduce the severity of the dam break waves.

Fig. 27 presents the time histories of the leading front position of the

fluid-particle flows in different cases. Similar conclusions can be drawn from the simulation of liquid-solid dam-break flows interaction impacting a short square obstacle. Solid particles will slow down the
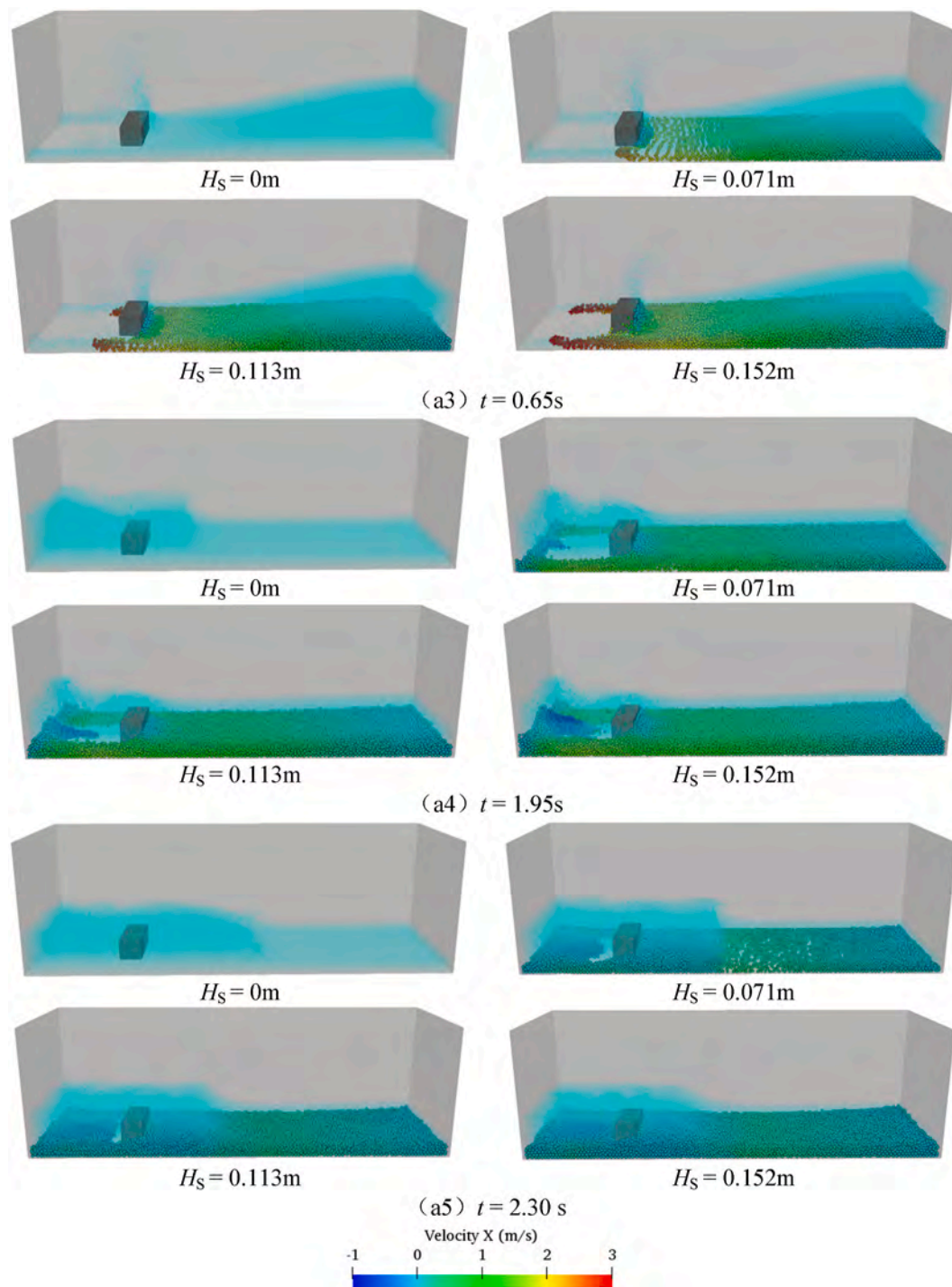
Fig. 17. (*continued*).

movement speed of the fluid front. The more particles there are, the slower the fluid front moves. Conversely, the more solid particles there are, the faster the sediment front moves. Additionally, it can be observed that the square column does not significantly affect the movement of the fluid-particle two-phase flow front.

5. Concluding remarks

In this paper, a new unresolved MPS-DEM coupling method is developed to simulate the interaction between the liquid-solid dam-break flows and rigid structures. This method fully utilises the advantages of MPS in capturing complex free-surfaces and the ability of DEM

in simulating solid collisions. Two benchmarks are simulated to evaluate the performance of the present method. Two MPS-DEM models with different formulations, referred to as Models A and B are compared in detail. Then, the MPS-DEM method is employed to investigate the liquid-solid dam-break flows impacting rigid structures. The key conclusions drawn are as follows:

(i) In the first example of multiple particle sedimentation, the kinetic energy, pressure, and fluid forces are recorded. The kinetic energy of the whole of solid particles falls close to zero and the fluid pressure is very smooth in the simulation with Model B, while the kinetic energy increases and pressure oscillates more violently in
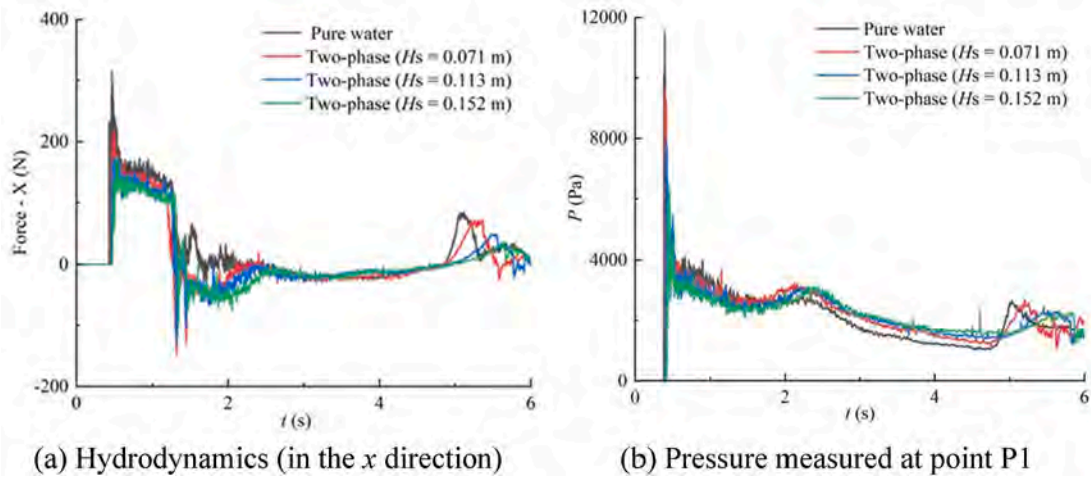
(a) Hydrodynamics (in the *x* direction)

(b) Pressure measured at point P1

Fig. 18. Time histories of hydrodynamic loads exerted on the square obstacle - liquid-solid dam-break flows with a short obstacle.
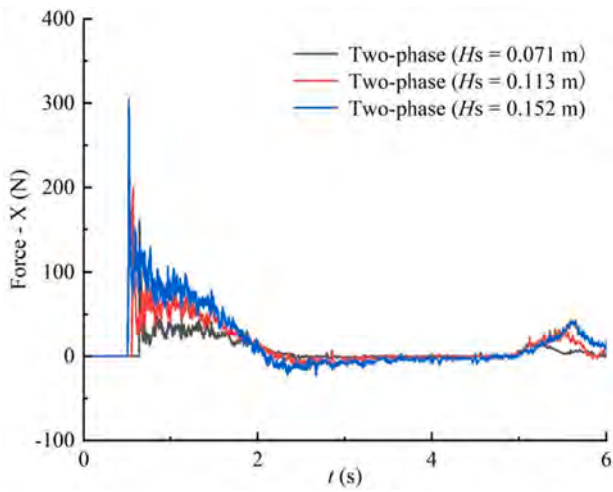

Fig. 19. Time histories of the loads of solid particles exerted on the square obstacle in the X direction - liquid-solid dam-break flows with a short obstacle.
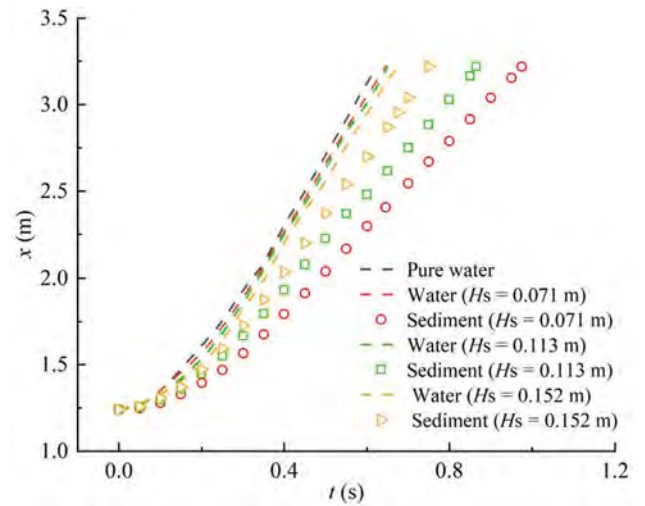

Fig. 21. Time histories of the leading front of the fluid-particle flows - liquid-solid dam-break flows with a short obstacle.
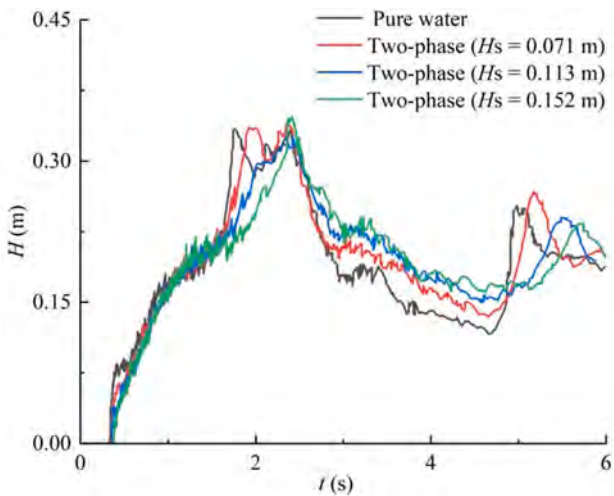

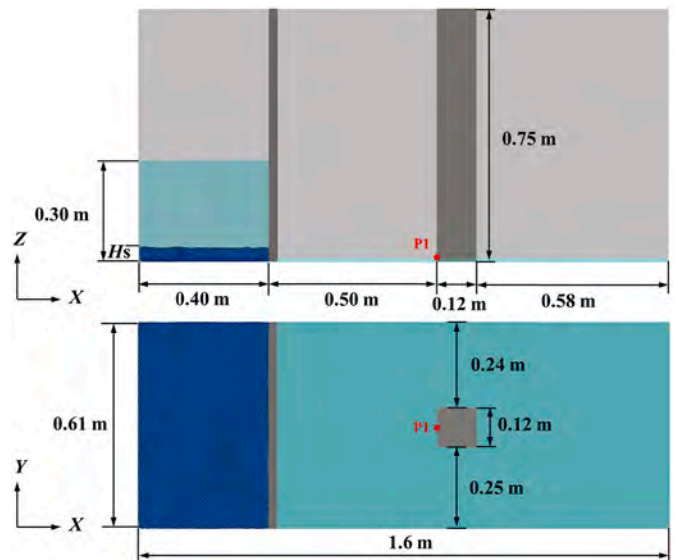**Fig. 20.** Time histories of the wave height at H1 - liquid-solid dam-break flows with a short obstacle.

Fig. 22. The sketch of the model - liquid-solid dam-break flows with a square column.
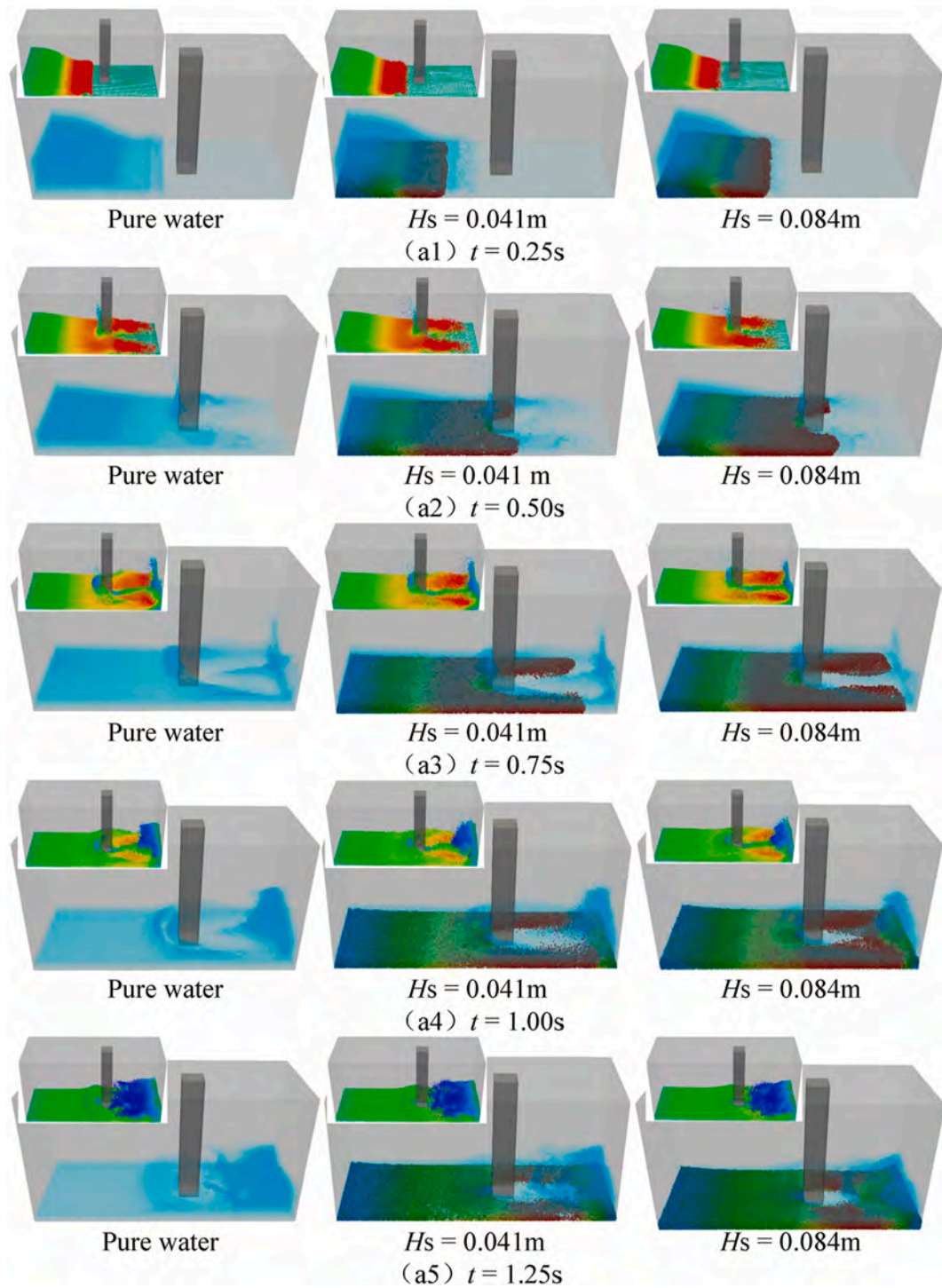
Fig. 23. Simulation snapshots obtained by MPS-DEM - liquid-solid dam-break flows with a vertical square column.
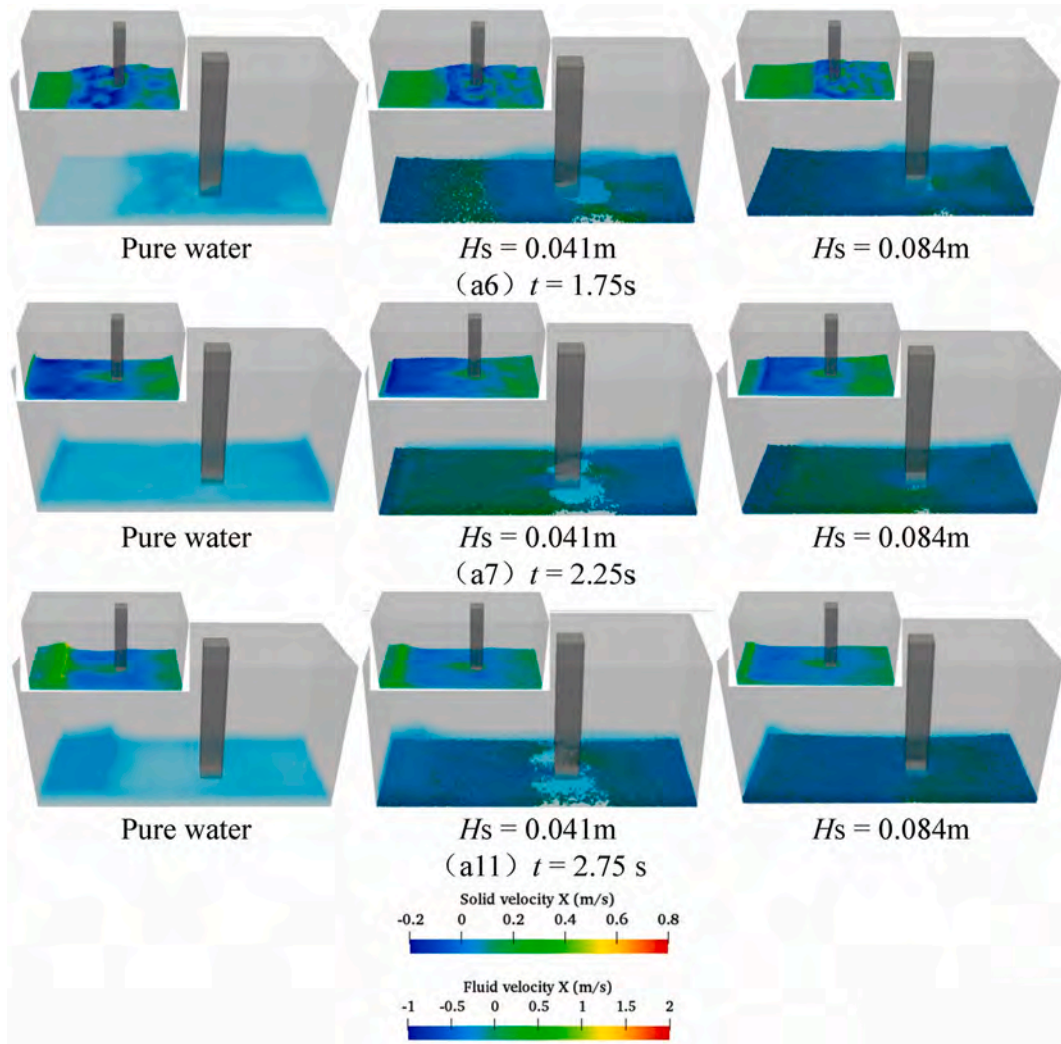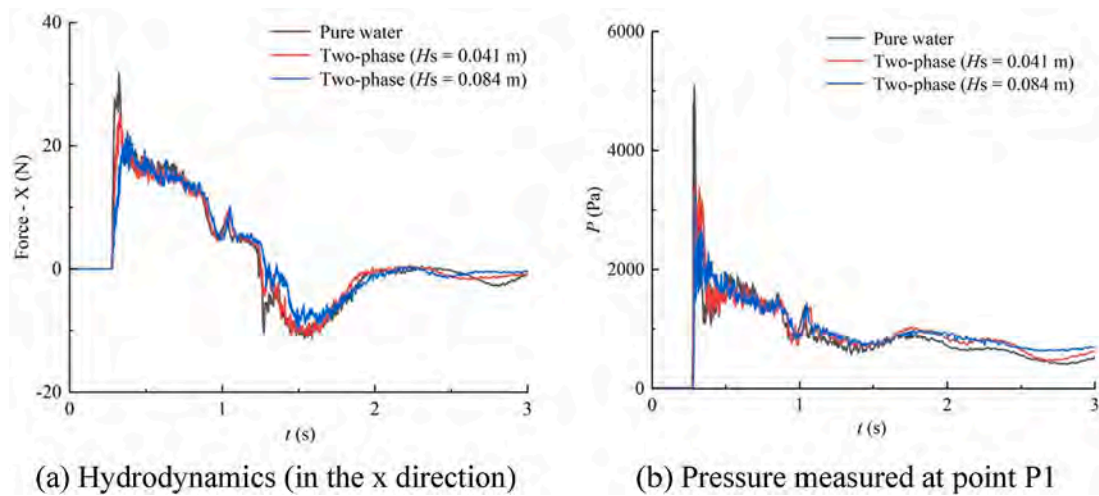
Fig. 23. (*continued*).

(a) Hydrodynamics (in the x direction)

(b) Pressure measured at point P1

Fig. 24. Time histories of the hydrodynamic loads exerted on the square column - liquid-solid dam-break flows with a vertical square column.
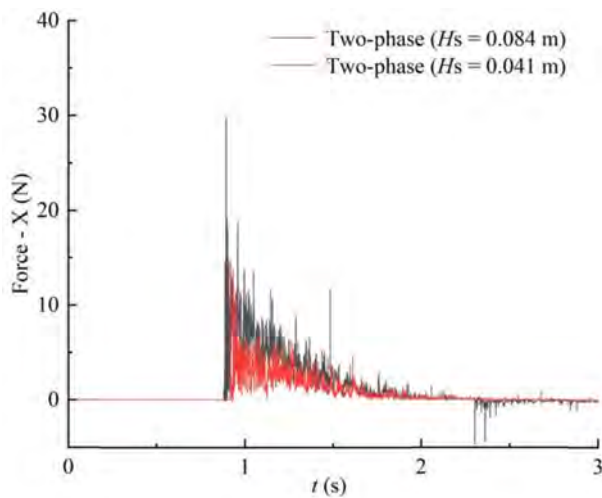
Fig. 25. Time histories of the loads of the solid particles exerted on the square column in the X direction - liquid-solid dam-break flows with a vertical square column.
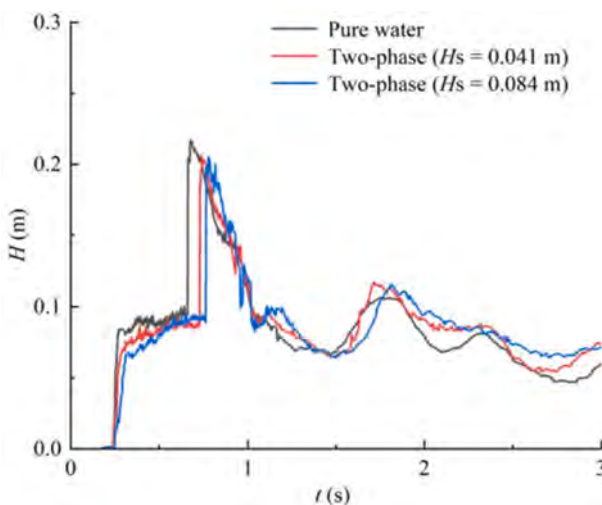

Fig. 26. Time histories of the wave height at the H1 - liquid-solid dam-break flows with a vertical square column.

Fig. 27. Time histories of the leading front position of the fluid-particle flows - liquid-solid dam-break flows with a vertical square column.

of sediment movement increases. In the cases with the maximum solid particle concentration, the peak pressure is the smallest, while the impact force exerted by the solid particles is the largest. Furthermore, solid sediment can significantly reduce the severity of dam-break waves.

The results show that the proposed MPS-DEM coupling method may provide a potential tool to simulate the interaction between the liquid-solid flows and rigid structures. In the future, liquid-solid two-phase flows with irregularly shaped particles will be considered. In addition, a multi-GPUs acceleration technique with MPI parallel strategy will be introduced to the MPS-DEM coupling method to improve its efficiency.

CRediT authorship contribution statement

Fengze Xie: Writing – original draft, Visualization, Validation, Software, Methodology, Investigation, Formal analysis, Data curation, Conceptualization. **Guohua Pan:** Writing – original draft, Visualization, Validation, Data curation. **Weiwen Zhao:** Writing – review & editing, Visualization, Software, Investigation, Data curation. **Decheng Wan:** Writing – review & editing, Supervision, Resources, Project administration, Methodology, Funding acquisition, Conceptualization.

Data availability

The data that support the findings of this study are available from the corresponding author upon reasonable request.

Declaration of competing interest

The authors declare that they have no known competing financial interests or personal relationships that could have appeared to influence the work reported in this paper.

Acknowledgments

the simulation with Model A. Besides, the drag force exerted on the solid tends to be zero in the simulation with Model B, which is almost identical to the theoretical solution. But both the drag force and the pressure gradient force in the simulation with Model A show significant discrepancies compared to the theoretical solution.

(ii) In the second example of two-phase dam-break flows, the shape of the sediment, the profile of free-surface, and the leading front of flows simulated by the 3D MPS-DEM with Model B are in good agreement with those in experiment, whereas the surface of the sediment is uneven in the simulation with Model A. In summary, the 3D MPS-DEM with Model B performs better than the 3D MPS-DEM with Model A in terms of accuracy and stability.

(iii) In the examples of liquid-solid dam-break flows with rigid structures, as the concentration of solid particles increases, the evolution rate of the dam-break flow decreases, while the velocity
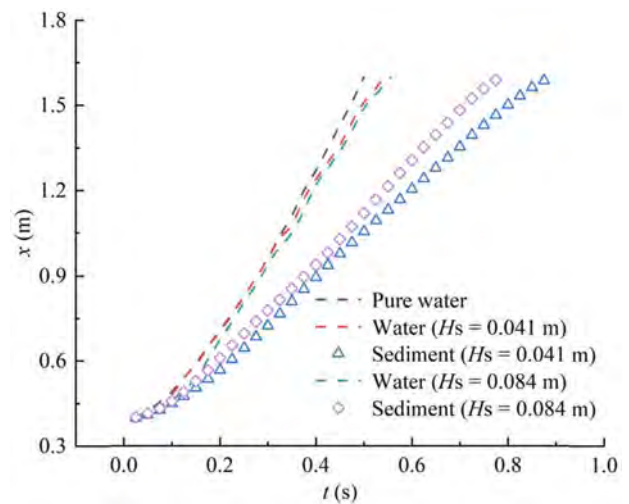
Appendix

In the MPS-DEM, the fluid phase is regarded as a continuous phase. Its flow follows the law of conservation of mass and momentum when expressed in terms of local-average variables (Feng and Yu, 2004). Two formulations, namely models A and B, have been proposed by Gidaspow (1994). Model A assumes that the pressure drop is shared between the fluid and solid phases, while model B assumes that it is only exerted on the fluid phase. In the present appendix, the detailed derivation process of the PPE source term will be provided.

The governing equations (Model A) for the fluid phase in liquid-solid flows is given by, (A)

$$\frac{D\varepsilon_f \rho_f}{Dt} + \rho_f \nabla \bullet \boldsymbol{u}_d = 0 \tag{A.1}$$

$$\rho_f \frac{D\boldsymbol{u}_d}{Dt} = -\varepsilon_f \nabla P + \mu_f \nabla^2 \boldsymbol{u}_d - \boldsymbol{f}_A + \varepsilon_f \rho_f \boldsymbol{g} \tag{A.2}$$

The time derivative in Eq. (A. 2) can be discretized in the following form, given by,

$$\frac{D\boldsymbol{u}_d}{Dt} = \frac{\boldsymbol{u}_d^{m+1} - \boldsymbol{u}_d^m}{\Delta t} = -\frac{\varepsilon_f}{\rho_f} \nabla P + \frac{\mu_f}{\rho_f} \nabla^2 \boldsymbol{u}_d - \frac{\boldsymbol{f}_A}{\rho_f} + \varepsilon_f \boldsymbol{g} \tag{A.4}$$

An intermediate velocity $\boldsymbol{u}_d^*$, corresponding to an intermediate density ρ_f^* is introduced. Thus, Eq. (A. 4) can be decomposed into two parts, given by,

$$\boldsymbol{u}_d^{m+1} - \boldsymbol{u}_d^* = -\frac{\varepsilon_f \Delta t}{\rho_f} \nabla P^{m+1} \tag{A.5}$$

$$\boldsymbol{u}_d^* - \boldsymbol{u}_d^m = \left(\frac{\mu_f}{\rho_f} \nabla^2 \boldsymbol{u}_d - \frac{\boldsymbol{f}_A}{\rho_f} + \varepsilon_f \boldsymbol{g} \right) \bullet \Delta t \tag{A.6}$$

By taking the gradient of both sides of Eq. (A.5), Eq. (A.5) is rewritten as,

$$\nabla \boldsymbol{u}_d^{m+1} - \nabla \boldsymbol{u}_d^* = -\frac{\varepsilon_f \Delta t}{\rho_f} \nabla^2 P^{m+1} \tag{A.7}$$

The first term on left hand side of Eq. (A. 7) is equal to zero. Thus, Eq. (A. 7) can be reformulated as,

$$\nabla^2 P^{m+1} = \frac{\rho_f}{\varepsilon_f \Delta t} \nabla \bullet \boldsymbol{u}_d^* \tag{A.8}$$

The time derivative in Eq. (A. 1) can be discretized in the following form, given by,

$$\frac{\varepsilon_f \rho_f^{m+1} - \varepsilon_f \rho_f^m}{\Delta t} = -\rho_f \nabla \bullet \left(\boldsymbol{u}_d^{m+1} - \boldsymbol{u}_d^* + \boldsymbol{u}_d^* \right) \tag{A.9}$$

$$\frac{\varepsilon_f \rho_f^{m+1} - \varepsilon_f \rho_f^*}{\Delta t} = -\rho_f \nabla \bullet \left(\boldsymbol{u}_d^{m+1} - \boldsymbol{u}_d^* \right) \tag{A.10}$$

By substituting equation Eq. (A. 5) into equation Eq. (A. 10), another source term can be obtained, given by,

$$\nabla^2 P^{m+1} = \rho_f \frac{\rho_f^{m+1} - \rho_f^*}{\rho_f \Delta t^2} = -\frac{\rho_f}{\Delta t^2} \frac{\langle n^* \rangle_i - n^0}{n^0} \tag{A.11}$$

The mixed source term can be rewritten as,

$$\langle \nabla^2 p^{m+1} \rangle_i = (1 - \gamma) \frac{\rho_f}{\Delta t} \nabla \bullet \boldsymbol{u}_i^* - \gamma \frac{\rho_f}{\Delta t^2} \frac{\langle n^m \rangle_i - n^0}{n^0} \tag{A 12}$$

Similar to the derivation process of Model A, the mixed source term in Model B can be expressed as,

$$\langle \nabla^2 p^{m+1} \rangle_i = (1 - \gamma) \frac{\varepsilon_f \rho_f}{\Delta t} \nabla \bullet \boldsymbol{u}_i^* - \gamma \frac{\varepsilon_f \rho_f}{\Delta t^2} \frac{\langle n^m \rangle_i - n^0}{n^0} \tag{B.1}$$

References

Anderson, T., Jackson, R., 1969. Fluid Mechanical Fluid mechanical description of fluidized beds. Comparison of theory and experiment. Ind. Eng. Chem. Fundam. 6 (4), 137–144.

Bu, S., Li, D., Chen, S., Xiao, C., Li, Y., 2022. Numerical simulation of landslide-generated waves using a SPH-DEM coupling model. Ocean Eng. 258.

Cundall, P., Strack, O., 1979. A discrete numerical model for granular assemblies. Geotechnique 29 (1), 47–65.

Duan, G., Koshizuka, S., Yamaji, A., Chen, B., Li, X., Tamai, T., 2018. An accurate and stable multiphase moving particle semi-implicit method based on corrective matrix for all particle interaction models. Int. J. Numer. Methods Eng. 115 (10), 1287–1314.

Ergun, S., 1952. Fluid flow through packed columns. Chem. Eng. Prog. 48, 89–94.

Feng, Y.Q., Yu, A.B., 2004. Assessment of model formulations in the discrete particle simulation of Gas−Solid flow. Ind. Eng. Chem. Res. 43 (26), 8378–8390.

Gidaspow, D., 1994. Multiphase Flow and Fluidization. Academic Press, San Diego.

Gingold, R., Monaghan, J., 1977. Smoothed particle hydrodynamics: theory and application to non-spherical stars, 181 (3), 375–389.

Gotoh, T., Khayyer, A., Gotoh, H., 2024. Enhanced schemes for resolution of the continuity equation in projection-based SPH. Eng. Anal. Bound. Elem. 166.

Harada, E., Gotoh, H., Ikari, H., Khayyer, A., 2019. Numerical simulation for sediment transport using MPS-DEM coupling model. Adv. Water Resour. 129, 354–364.

Harada, E., Ikari, H., Shimizu, Y., Khayyer, A., Gotoh, H., 2018. Numerical investigation of the morphological dynamics of a step-and-pool riverbed using DEM-MPS. Journal of Hydraulic Enginneering 144 (1), 04017058.

He, Y., Bayly, A.E., Hassanpour, A., Muller, F., Wu, K., Yang, D., 2018. A GPU-based coupled SPH-DEM method for particle-fluid flow with free surfaces. Powder Technol. 338, 548–562.

Hu, K.C., Hsiao, S.C., Hwung, H.H., Wu, T.R., 2012. Three-dimensional numerical modeling of the interaction of dam-break waves and porous media. Adv. Water Resour. 47, 14–30.

Jandaghian, M., Krimi, A., Shakibaeinia, A., 2021. Enhanced weakly-compressible MPS method for immersed granular flows. Adv. Water Resour. 152, 103908.

Jin, Z.H., Wei, F.F., Wu, Y.W., Qu, K., Luo, X., Ren, X.Y., 2023. Simulations of debris flow impacting on bridge pier based on coupled CFD-DEM method. Ocean Eng. 279.

Khayyer, A., Gotoh, H., 2010. A higher order Laplacian model for enhancement and stabilization of pressure calculation by the MPS method. Appl. Ocean Res. 32 (1), 124–131.

Khayyer, A., Gotoh, H., 2011. Enhancement of stability and accuracy of the moving particle semi-implicit method. J. Comput. Phys. 230 (8), 3093–3118.

Khayyer, A., Gotoh, H., 2012. A 3D higher order Laplacian model for enhancement and stabilization of pressure calculation in 3D MPS-based simulations. Appl. Ocean Res. 37, 120–126.

Khayyer, A., Gotoh, H., Shimizu, Y., 2017. Comparative study on accuracy and conservation properties of two particle regularization schemes and proposal of an optimized particle shifting scheme in ISPH context. J. Comput. Phys. 332, 236–256.

Khayyer, A., Shimizu, Y., Gotoh, T., Gotoh, H., 2023. Enhanced resolution of the continuity equation in explicit weakly compressible SPH simulations of incompressible free-surface fluid flows. Appl. Math. Model. 116, 84–121.

Kleefsman, K.M.T., Fekken, G., Veldman, A.E.P., Iwanowski, B., Buchner, B., 2005. A Volume-of-Fluid based simulation method for wave impact problems. J. Comput. Phys. 206 (1), 363–393.

Koshizuka, S., Oka, Y., 1996. Moving-particle semi-implicit method for fragmentation of incompressible fluid. Nucl. Sci. Eng. 123 (3), 421–434.

Li, J., Qiu, L., Tian, L., Yang, Y., Han, Y., 2019. Modeling 3D non-Newtonian solid–liquid flows with a free-surface using DEM-MPS. Eng. Anal. Bound. Elem. 105, 70–77.

Liu, X., Wang, K., Duan, G., Zhang, S., 2024. A volume-conservation particle shifting scheme for moving particle method simulating free-surface flow. Computational Particle Mechanics 11 (6), 2857–2868.

Lyu, H., Sun, P., 2022. Further enhancement of the particle shifting technique: towards better volume conservation and particle distribution in SPH simulations of violent free-surface flows. Appl. Math. Model. 101, 214–238.

Markauskas, D., Kruggel-Emden, H., Scherer, V., 2018. Numerical analysis of wet plastic particle separation using a coupled DEM-SPH method. Powder Technol. 325, 218–227.

Meng, W., Yu, C., Li, J., An, R., 2022. Three-dimensional simulation of silted-up dam-break flow striking a rigid structure. Ocean Eng. 261.

Pahar, G., Dhar, A., 2017. Numerical modelling of free-surface flow-porous media interaction using divergence-free moving particle semi-implicit method. Transport Porous Media 118 (2), 157–175.

Ren, B., Wen, H., Dong, P., Wang, Y., 2016. Improved SPH simulation of wave motions and turbulent flows through porous media. Coast. Eng. 107, 14–27.

Sakai, M., Shigeto, Y., Sun, X., Aoki, T., Saito, T., Xiong, J., Koshizuka, S., 2012. Lagrangian–Lagrangian modeling for a solid–liquid flow in a cylindrical tank. Chem. Eng. J. 200–202, 663–672.

Shimizu, Y., Gotoh, H., 2024. Volume-conserved wavy interface boundary for δ-SPH-based numerical wave flume. Coast. Eng. J. 1–18.

Sun, J., Zou, L., Govender, N., Martínez-Estévez, I., Crespo, A.J.C., Sun, Z., Domínguez, J.M., 2023. A resolved SPH-DEM coupling method for analysing the interaction of polyhedral granular materials with fluid. Ocean Eng. 287.

Sun, J., Zou, L., Govender, N., Sun, Z., Yu, Z., Jin, G., 2024. Coupling SPH-DEM method for simulating the dynamic response of breakwater structures under severe free surface flow. Powder Technol. 441.

Sun, P.N., Le Touzé, D., Oger, G., Zhang, A.M., 2021. An accurate FSI-SPH modeling of challenging fluid-structure interaction problems in two and three dimensions. Ocean Eng. 221.

Sun, X., Sakai, M., 2015. Three-dimensional simulation of gas–solid–liquid flows using the DEM–VOF method. Chem. Eng. Sci. 134, 531–548.

Sun, X., Sakai, M., Sakai, M.-T., Yamada, Y., 2014. A Lagrangian–Lagrangian coupled method for three-dimensional solid–liquid flows involving free surfaces in a rotating cylindrical tank. Chem. Eng. J. 246, 122–141.

Sun, X., Sakai, M., Yamada, Y., 2013. Three-dimensional simulation of a solid–liquid flow by the DEM–SPH method. J. Comput. Phys. 248, 147–176.

Tanaka, M., Masunaga, T., 2010. Stabilization and smoothing of pressure in MPS method by Quasi-Compressibility. J. Comput. Phys. 229 (11), 4279–4290.

Tang, X., Wang, S., Shen, Y., 2024. Super-quadric CFD-DEM-VOF modelling of gas–solid-liquid systems. Adv. Powder Technol. 35 (1), 104282.

Tang, Y., Jiang, Q., Zhou, C., 2018. A Lagrangian-based SPH-DEM model for fluid–solid interaction with free surface flow in two dimensions. Appl. Math. Model. 62, 436–460.

Tazaki, T., Harada, E., Gotoh, H., 2023. Grain-scale investigation of swash zone sediment transport on a gravel beach using DEM-MPS coupled scheme. Coast. Eng. J. 65 (2), 347–368.

Tazaki, T., Harada, E., Gotoh, H., 2024. Coherent turbulent flow structure under plunging breaker on movable grain bed simulated by 3D DEM-MPS method. Coast. Eng. J. 66 (4), 675–702.

Thornton, C., Randall, C., 1988. Applications of theoretical contact mechanics to solid particle system simulation. In: Satake, M., Jenkins, T.J. (Eds.), Micromechanics Granular Matters. Elsevier, Amsterdam, pp. 133–142.

Wen, C., Yu, Y., 1966. Mechanics of fluidization. Chem. Eng. Prog. Symp. Ser. 62, 100–111.

Wen, H., Ren, B., Wang, G., 2018. 3D SPH porous flow model for wave interaction with permeable structures. Appl. Ocean Res. 75, 223–233.

Xie, F., Meng, Q., Wan, D., 2022. Numerical simulations of liquid-solid flows in A vertical pipe by MPS-DEM coupling method. China Ocean Eng. 36 (4), 542–552.

Xie, F., Zhao, W., Wan, D., 2021. Numerical simulations of liquid-solid flows with free surface by coupling IMPS and DEM. Appl. Ocean Res. 114.

Yu, R., Dong, X., Li, Z., Fan, M., 2023. A coupled SPH–DEM model for erosion process of solid surface by abrasive water-jet impact. Computational Particle Mechanics 10 (5), 1093–1112.

Zhang, S., Kuwabara, S., Suzuki, T., Kawano, Y., Morita, K., Fukuda, K., 2009. Simulation of solid–fluid mixture flow using moving particle methods. J. Comput. Phys. 228 (7), 2552–2565.

Zhang, Y., Hou, S., Di, S., Liu, Z., Xu, Y., 2023. DEM–SPH coupling method for landslide surge based on a GPU parallel acceleration technique. Comput. Geotech. 164.

Zhang, Y., Wan, D., Hino, T., 2014. Comparative study of MPS method and level-set method for sloshing flows. J. Hydrodyn. 26 (4), 577–585.

Zhou, Z.Y., Kuang, S.B., Chu, K.W., Yu, A.B., 2010. Discrete particle simulation of particle–fluid flow: model formulations and their applicability. J. Fluid Mech. 661, 482–510.

Zhu, H.P., Zhou, Z.Y., Yang, R.Y., Yu, A.B., 2007. Discrete particle simulation of particulate systems: theoretical developments. Chem. Eng. Sci. 62 (13), 3378–3396.